Synthesis and combustion inhibition efficiency of iron short-chain perfluorocarboxylates

Yusuke Koshiba [a, 1*], Yuji Tsunokuma [b, 1], Hideo Ohtani [c]

[a] Department of Materials Science and Chemical Engineering, Faculty of Engineering, Yokohama National University, 79-5 Tokiwadai, Hodogaya-ku, Yokohama 240-8501, Japan

[b] Graduate School of Environmental and Information Sciences, Yokohama National University, 79-7 Tokiwadai, Hodogaya-ku, Yokohama 240-8501, Japan

[c] Department of Safety Management, Faculty of Environmental and Information Sciences, Yokohama National University, 79-7 Tokiwadai, Hodogaya-ku, Yokohama 240-8501, Japan

* Corresponding author: E-mail address: koshiba-yusuke-xm@ynu.ac.jp

                            Complete postal address: 79-5 Tokiwadai, Hodogaya-ku, Yokohama 240-8501, Japan

1: These authors contributed equally to this work and should be considered as co-first authors.

Abstract

This study reports an experimental exploration of the combustion inhibition efficiency of iron short-chain perfluorocarboxylates, namely, iron trifluoroacetate (FeTFA) and iron pentafluoropropionate (FePFP). The aim is to develop a new phosphor-free fire-extinguishing agent. The synthesized FeTFA and FePFP were characterized by ultraviolet-visible spectroscopy, Fourier-transform infrared spectroscopy, X-ray fluorescence measurements, and fast-atom bombardment mass spectrometry. The FeTFA and FePFP ligands (i) coordinate with the iron ions in bridging form via carboxylate oxygens, (ii) contain no Cl^-, and (iii) are hexanuclear complexes with chemical formulas of $C_{18}F_{27}O_{22}Fe_6$ and $C_{27}F_{45}O_{22}Fe_6$, respectively. Suppression trials and thermogravimetric measurements revealed that (i) both FeTFA and FePFP have higher combustion inhibition ability at lower suppressant concentrations than ammonium dihydrogen phosphate (an active component in conventional fire-extinguishing agents), (ii) FePFP is remarkably more inhibition-efficient than FeTFA, and (iii) neither FeTFA nor FePFP hinder cellulose pyrolysis and char combustion in the condensed phase. Thermogravimetry–mass spectrometry measurements confirmed that (i) the main gas-phase decomposition product of FeTFA and FePFP is CF_3, and (ii) FePFP is a better CF_3 generator than FeTFA. The different inhibition abilities of the two complexes were attributed to their different CF_3 generation abilities and eases of decomposing the complex.

Keywords: Iron complex, Short-chain perfluorocarboxylato complex, Fire suppression, Minimum extinction concentration, Phosphorus-free, Flame inhibition, Powder fire-extinguishing agent

Nomenclature

Symbols

C_k Concentration of suppressant k (mol g^{-1})

c_p Fuel heat capacity (J g^{-1} K^{-1})

g Gravitational acceleration (9.8 m^2 s^{-1})

M Molar concentration (mol dm^{-3})

MEC   Minimum extinction concentration (mol g^{-1})

M_k Molar mass of suppressant k (g mol^{-1})

m/z Mass-to-charge ratio

n Carbon number of the perfluoroalkyl group

R Generation rate (ppm s^{-1}, ppm: mass/mass basis)

T Temperature (K)

U Downward flame spread rate (mm s^{-1})

V_k Normalized downward flame spread rate of the sample on which suppressant k was adsorbed

(dimensionless)

W Weight (mg)

Abbreviations

ADP   Ammonium dihydrogen phosphate

AFFF   Aqueous film forming foam

BCF   Bioconcentration factor

br   Broad

DFSR   Downward flame spread rate

DTG   First derivative of TG curve

FAB-MS   Fast-atom bombardment mass spectrometry

FeTFA   Iron trifluoroacetate

FePFP Iron pentafluoropropionate

FT-IR Fourier-transform infrared spectroscopy

HR High-resolution

LR Low-resolution

M Metal or third body

n Normal

NBA *m*-Nitrobenzyl alcohol

NMR Nuclear magnetic resonance

PFC Perfluorinated compound or perfluorocarboxylate (also known as perfluorocarboxylato complex)

PFCA Perfluorocarboxylic acid

PFOA Perfluorooctanoic acid

PFP Pentafluoropropionic acid or pentafluoropropionate

POPs Persistent organic pollutants

r.t. Room temperature

SC   Short-chain

SEM   Scanning electron microscopy

TFA   Trifluoroacetic acid or trifluoroacetate

TG   Thermogravimetry

TG–MS   Thermogravimetry–mass spectrometry

TLC   Thin-layer chromatography

UV–Vis   Ultraviolet–visible spectroscopy

XRF   X-ray fluorescence

Greek letters

δ Solid fuel thickness (mm) or chemical shift (ppm)

Δ Difference

ε Molar extinction coefficients ($dm^3\ mol^{-1}\ cm^{-1}$, $M^{-1}\ cm^{-1}$)

λ Gas phase thermal conductivity ($W\ cm^{-1}\ K^{-1}$)

λ_{max} Wavelength of maximum absorption (nm)

ρ_s Solid fuel density (g mm^{-3})

v Stretching vibration

Subscripts

as   Asymmetric

c   Complex

f   Flame

k   Suppressant or F-containing gas

o   Onset

r   Residual

s   Sample

sym   Symmetric

v   Vaporization

0   Pure

∞ Ambient

1. Introduction

According to Japan's fire statistics, the number of deaths, injuries, and economic losses caused by fires in 2019 amounted to 1,477, 5,814, and 80.2 billion yen, respectively. Gollner [1] mentioned that the proper use of an effective fire-extinguishing agent can reduce these fire-induced losses.

The active substance of a powder ABC fire-extinguishing agent is ammonium dihydrogen phosphate ($NH_4H_2PO_4$, ADP). Unfortunately, high-grade phosphate rock (phosphorite), a raw precursor material of ADP, has been depleted worldwide, and is now categorized as a critical raw material [2]. Although the depletion scenarios of economically exploitable phosphate rock resources depend on the consumption, conservation, and recycling of the resources, several recent studies report that phosphorus will be depleted by the twenty-second century at the earliest [3, 4]. Moreover, the phosphate rock market has been volatized by speculation (Fig. 1) [5]. This situation necessitates the development of a new phosphorus-free fire suppressant.
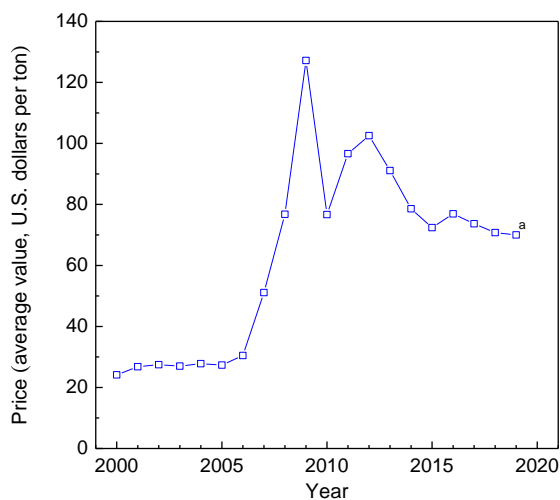
Figure 1

Trends in average market prices of phosphate rocks from 2000 to 2020 (adapted from [5]). a: Estimated.

Several metal compounds can scavenge the radicals in chain reactions within flames, thus behaving as effective fire suppressants. To date, several scholars have reported effective phosphorus-free agents. For instance, Ni et al. [6] developed transition metal compounds (Mn^{2+} and Cu^{2+}) supported on zeolite particles. Koshiba et al. found that the extinguishing abilities of chromocene ($Cr(C_5H_5)_2$) and manganocene ($Mn(C_5H_5)_2$) are 75 and 35 times higher, respectively, than that of ADP [7]. However, these compounds are minor metal compounds and toxic. Recent experiments on base-metal compounds have identified iron compounds as good suppressants. Linteris et al. demonstrated the high suppression efficiency of ferrocene ($Fe(C_5H_5)_2$) by measuring the burning velocities of premixed methane/air flames [8]. Koshiba et al. reported that ferrocene dispersions (oil-in-water

9

microemulsions and aqueous dispersions of fine ferrocene particles) more effectively extinguish pool

fires than a conventional extinguishing agent [9–11].

Perfluorinated compounds (PFCs) are common firefighting ingredients. Fukaya et al.'s *ab initio*

study [12] revealed that compounds with perfluoroalkyl groups partake in $CF_3\bullet$-catalyzed radical

recombination reactions. LeFort et al. investigated the fire suppression efficiency of water mists

containing Forafacs [13], while Magrabi et al. reported the drainage properties of aqueous film

forming foams (AFFFs) containing PFCs [14]. Perfluorocarboxylic acid (PFCA) is an organofluorine

compound with the chemical formula: $C_nF_{2n+1}CO_2H$. Unlike haloalkanes (e.g., Halons 1301 and 1211),

PFCAs have zero ozone depletion potentials. The major disadvantage of perfluorooctanoic acid

(PFOA, $n = 7$) is the toxicity of its salts. PFOA-related compounds are listed in the Stockholm

Convention on Persistent Organic Pollutants (POPs), because PFOAs are persistent, bioaccumulative,

and harmful to the environment and living organisms [15]. Prevedouros et al. [16] summarized the

global use and production of AFFF, and reported an estimated global AFFF emission of 50–100 t in

1965–1974. By contrast, short-chain ($n \leq 6$) PFCAs have insignificant bioconcentration factors [17],

so were delisted as POPs as of 2019.

As-is well-known in chemistry, carboxylates are common ligands that can bind iron ions.

According to the *principle of hard and soft acids and bases* (the so-called HSAB theory [18]), hard

acid Fe^{3+} prefers to coordinate with a hard base (e.g., carboxylate) than a soft base (e.g., phenanthroline

[19]). The main objectives of the present study were to (i) synthesize iron short-chain

perfluorocarboxylates (Fe-SCPFC, $n = 1$ and $n = 2$) and (ii) investigate their fire suppression efficiency.

The combination of iron with perfluorocarboxylates has not been previously reported in fire-related

research.

The remaining sections of this study proceed as follows. Section 2 explains the synthesis and

instrumental analysis of the iron perfluorocarboxylato complexes ($n = 1$ and $n = 2$). Hereafter, iron

trifluoroacetate (or trifluoroacetic acid, $n = 1$) and iron pentafluoropropionate (or pentafluoropropionic

acid, $n = 2$) are referred to as FeTFA and FePFP, respectively. Section 3 describes the combustion

inhibition efficiency of the synthesized Fe-SCPFCs, and Section 4 derives the suppression

mechanisms from thermogravimetry (TG) and TG-mass spectrometry (TG-MS) data. Section 5

concludes the study.

2.   Synthesis of Fe-SCPFCs

2.1 Chemicals

Iron (III) chloride ($FeCl_3$), TFA, and PFP (see Fig. 2) were of reagent grade with purities of >99.0%

(Junsei Chem. Co., Inc. (Japan), >98.0% (FUJIFILM Wako Pure Chem. Corp., Japan), and >97.0%

(FUJIFILM) respectively. They were used without further purification. All water was deionized (<1

μS cm^{-1}).
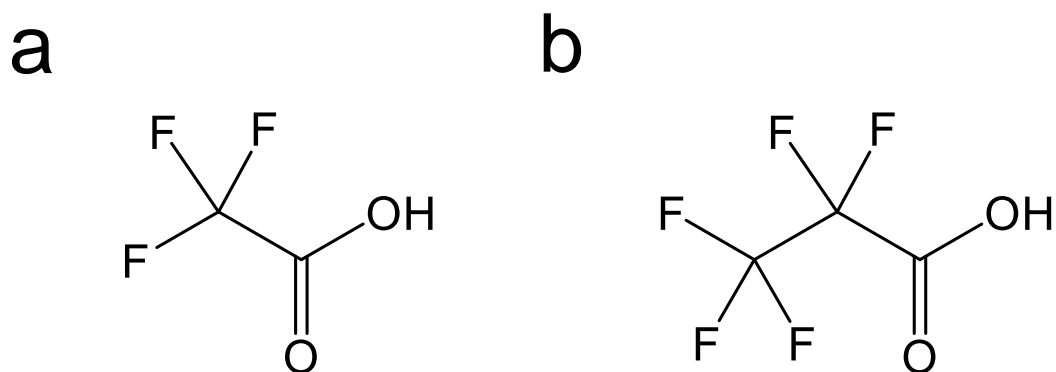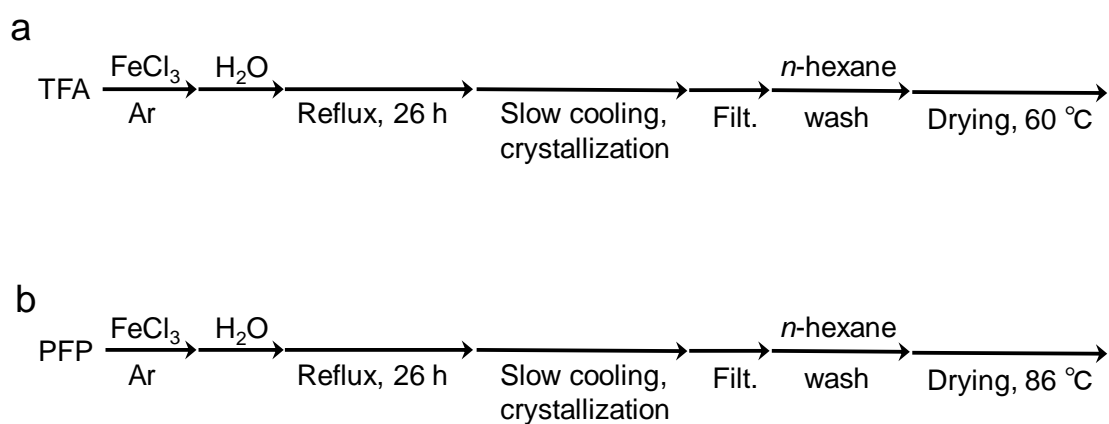

Figure 2

Chemical structures of (a) trifluoroacetic acid (TFA) and (b) pentafluoropropionic acid (PFP).

2.2 Synthesis methods of FeTFA and FePFP

2.2.1 Preparation of FeTFA

An oven-dried two-necked round-bottom flask was charged with FeCl$_3$ (5.0 g, 31 mmol) and

excess TFA (5.0×10^{-2} dm^3, 0.65 mol, 21 mol. *eq*.). When supplied in excess, TFA was both reactant

and solvent. Water (5.0×10^{-4} dm^3) was then added dropwise to dissolve the FeCl$_3$. The mixture was

stirred (400 rpm) under reflux for 26 h. The reaction proceeded under an Ar atmosphere and was

monitored on cellulose thin-layer chromatography (TLC) plates (TLC Cellulose F, Merck). After slow

cooling to room temperature (r.t.) to precipitate the crystals, the mixture was filtered and washed with

n-hexane, then dried in a vacuum desiccator for >5 h at 60 °C to remove the TFA. The FeTFA product

(7.82 g) was obtained as dark red hexahedron crystals (Scheme 1a; Fig. 3a).

a

$$\text{TFA} \xrightarrow[\text{Ar}]{\text{FeCl}_3, \text{ H}_2\text{O}} \xrightarrow{\text{Reflux, 26 h}} \xrightarrow[\substack{\text{Slow cooling,}\\\text{crystallization}}]{} \xrightarrow{\text{Filt.}} \xrightarrow[\text{wash}]{\textit{n}\text{-hexane}} \xrightarrow{\text{Drying, 60 }^{\circ}\text{C}}$$

b

$$\text{PFP} \xrightarrow[\text{Ar}]{\text{FeCl}_3, \text{ H}_2\text{O}} \xrightarrow{\text{Reflux, 26 h}} \xrightarrow[\substack{\text{Slow cooling,}\\\text{crystallization}}]{} \xrightarrow{\text{Filt.}} \xrightarrow[\text{wash}]{\textit{n}\text{-hexane}} \xrightarrow{\text{Drying, 86 }^{\circ}\text{C}}$$

Scheme 1 Synthesis methods of (a) FeTFA (water/TFA, reflux, 26 h) and (b) FePFP (water/PFP, reflux,

26 h).
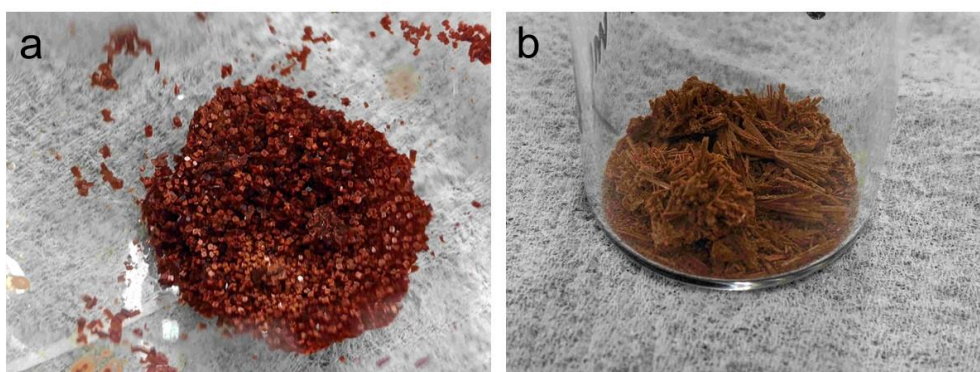
Figure 3

Appearance of synthesized (a) FeTFA (dark red hexahedron crystals in a dry N_2 purged vial) and (b)

FePFP (dark orange needle-like crystals in a dry N_2 purged vial).

2.2.2   Preparation of FePFP

An oven-dried two-necked round-bottom flask was charged with $FeCl_3$ (5.0 g, 31 mmol), and PFP

(as both reactant and solvent) was added in excess (5.0×10^{-2} dm^3, 0.48 mol, 15.5 mol. *eq*.). The $FeCl_3$

was then dissolved by dropwise addition of water (5.0×10^{-4} dm^3). The mixture was stirred (400 rpm)

at the reflux temperature for 26 h in Ar, then analyzed by cellulose TLC (TLC Cellulose F, Merck).

After slow cooling to r.t., the precipitate was filtered, washed with *n*-hexane, and then dried under

reduced pressure for >5 h at 86 °C. The FePFP product (11.1 g) was obtained as dark orange needle-

like crystals (Scheme 1b; Fig. 3b).

2.3 Characterization methods

Melting point: The melting points of synthesized FeTFA and FePFP were measured using an ATM-

02 melting point measuring instrument (AS ONE, Japan) under a dry N_2 atmosphere ($H_2O < 15$ ppm).

Ultraviolet–visible spectroscopy (UV–Vis): The coordination of the ligands (i.e., trifluoroacetate

and pentafluoropropionate) with the metal (i.e., iron ions) was determined from UV–Vis

14

measurements. The UV–Vis spectra of aqueous FeTFA and FePFP solutions were recorded on a UV–Vis spectrophotometer (Jasco V560, Japan) in the wavelength range 200–800 nm. The solute concentrations were 1.00×10^{-4} M in 1-cm quartz cells. The measurements yielded the wavelengths of maximum absorption (λ_{max}, nm) and the molar extinction coefficients (ε, $dm^3\ mol^{-1}\ cm^{-1}$).

Fourier-transform infrared spectroscopy (FT-IR): The ligands' iron-binding sites were determined by FT-IR. The infrared spectra were recorded with an FT-IR spectrometer (Jasco FT-IR 6200, Japan) using KBr disks (16 scans).

X-ray fluorescence (XRF): The absence or presence of $FeCl_3$ residues (the starting reactant) in the synthesized FeTFA and FePFP was checked by XRF (JSX-3100RII, JEOL Ltd., Japan) with an Al filter [20]. In addition, Cl^- ions were detected in an elution test following a standard method [21] based on ion chromatography.

Fast-atom bombardment mass spectrometry (FAB-MS): The molecular masses and chemical structures of the synthesized FeTFA and FePFP were verified by FAB-MS (mass spectrometer, JEOL JMS-700N, Japan; ion mode, positive; output m/z range, 50–1,800). Ionization of a sample by FAB-MS generally requires a matrix to prevent the evaporation of ions under the high-vacuum conditions; in this study, the matrix was *m*-nitrobenzyl alcohol (NBA).

2.4 Characterization results of FeTFA and FePFP

2.4.1 Melting points

Both FeTFA and FePFP were obtained at approximately 100% yield. As the FeTFA and FePFP complexes are highly hygroscopic, we attempted to measure their melting points (as a check of their purities) under a dry N_2 atmosphere. Unfortunately, no melting points were observed (Fig. S1). FeTFA and FePFP visually decomposed at ca. 140 °C, as supported by the color change and volume decrease of the crystals during the measurements. This result was consistent with the TG and TG–MS results (see Section 4).

2.4.2 UV–Vis measurements

FeCl$_3$ displayed two main absorption bands at λ_{max} = 245 nm (ε = 3.88 dm^3 mol^{-1} cm^{-1}) and 359 nm (ε = 3.78 dm^3 mol^{-1} cm^{-1}). No absorption bands in the spectra of TFA and PFP (i.e., the ligands) were observed at >350 nm [22]. FeTFA yielded absorption bands at λ_{max} = 322 nm (ε = 4.09 dm^3 mol^{-1} cm^{-1}) and 474 nm (ε = 2.47 dm^3 mol^{-1} cm^{-1}), while FePFP yielded absorption bands at λ_{max} = 304 nm (ε = 3.91 dm^3 mol^{-1} cm^{-1}) and 497 nm (ε = 2.66 dm^3 mol^{-1} cm^{-1}). Comparisons of the complex's spectra with the ligand spectra reveal a redshift of the higher-energy band, and new absorption bands at 474 and 497 nm appeared in the spectra of FeTFA and FePFP, respectively. The charge–transfer bands are responsible for the colors of these complexes, supporting the observation that the ligands

16

were coordinated with iron ions.

2.4.3 FT-IR measurements

The FT-IR spectrum of pure TFA displayed bands at around 3,200, 1,783, 1,447, and 1,170 cm^{-1}, corresponding to the stretching frequency of the O–H bonds, asymmetric stretching (v_{as}) of the CO_2^- group, symmetric stretching (v_{sym}) of the CO_2^- group, and stretching vibrations of the C–F bonds, respectively [23, 24]. The corresponding bands of pure PFP are 3,200, 1,744, 1,434, and 1,162 cm^{-1}, respectively [23]. The infrared spectra of the synthesized FeTFA and FePFP are shown in Fig. 4a and 4b, respectively. After complexation, CO_2^- asymmetric stretching of FeTFA and FePFP appeared at around 1,655 and 1,678 cm^{-1}, respectively. The observed redshifting confirmed that these ligands coordinated with the iron ions via carboxylate oxygens, mainly because the decreased electron density of the CO_2^- groups after complexation lowered the absorption frequency.

a

b
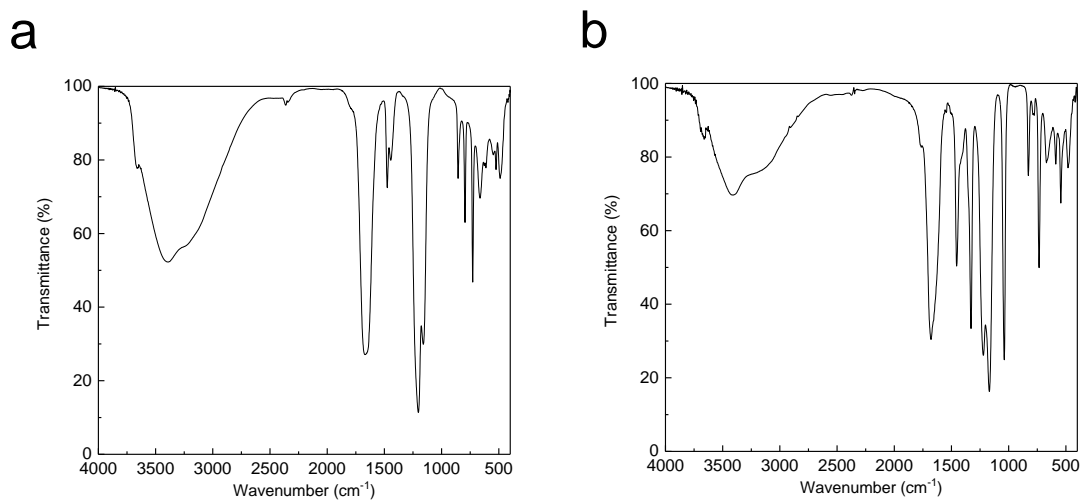
Figure 4

FT-IR spectra (KBr, r.t.) of (a) FeTFA and (b) FePFP.

From the differences in the CO_2^- group frequencies ν_{as} and ν_{sym} ($\Delta\nu = \nu_{as} - \nu_{sym}$), we determined

the coordination types of the CO_2^- group complexed with metal ions. Typical coordination structures

are *unidentate*, *bidentate*, *chelating*, and *bridging* (Fig. S2). The $\Delta\nu$ values are roughly ordered as

unidentate > ionic > bridging > bidentate chelating [25, 26]. In the infrared data of M trifluoroacetate

(M: metal cation), Deacon and Phillips [26] reported $\Delta\nu$ values of 147–245, 202, and 264–382 cm^{-1}

for the *bridging*, *ionic*, and *unidentate* coordinations, respectively. As shown in Fig. 4, the $\Delta\nu$ value of

the synthesized FeTFA was approximately 200 cm^{-1}. This result strongly suggests that although the

ionic form cannot be denied, TFAs coordinated with the iron ions in the bridging form.

18

2.4.4   XRF measurements and Cl⁻ elution tests

Cl is a well-known flame inhibitor [27, 28]. As noted in Section 3, the combustion inhibition

abilities of FeTFA and FePFP cannot be accurately evaluated if these synthesized complexes contain

$FeCl_3$ residues and Cl^- ions.

Elemental XRF analysis of the synthesized FeTFA and FePFP detected only Fe (100%) (Fig. 5). It

must be noted that the Rh peaks (e.g., the ca. 2.7 eV peak) arose from the Rh tube. The elution test

also revealed the absence of Cl^- ions ($<10^{-3}$ wt%, below the detection limit of XRF) in the synthesized

FeTFA and FePFP.

In summary, no Cl^- impurity was present in the FeTFA and FePFP complexes, meaning that the

combustion inhibition efficiency of the complexes could be evaluated without inhibition by chlorine.
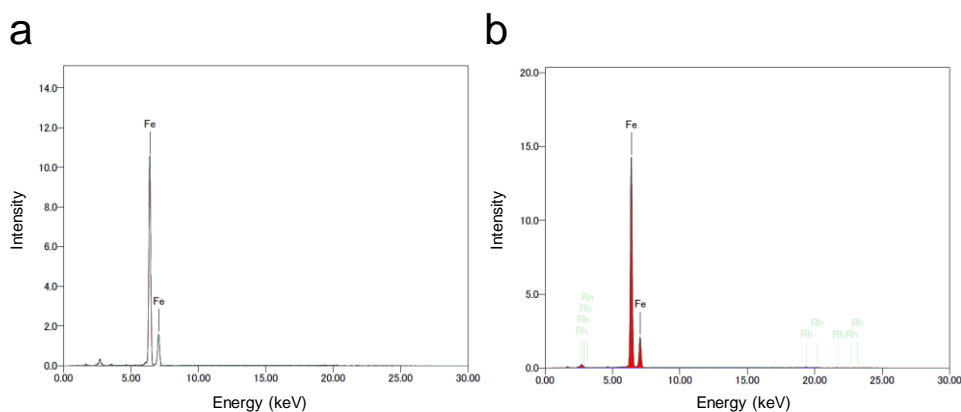
Figure 5

XRF spectra of (a) FeTFA and (b) FePFP (30.0 kV). The rhodium peaks are contributed by the Rh

tube.

2.4.5   FAB-MS measurements

Elemental analysis and single-crystal X-ray diffraction (XRD) studies directly determine the

elemental composition and chemical structure (e.g., bond length and angle) of a synthesized sample.

Unfortunately, these analyses were precluded by the high hygroscopicity of FeTFA and FePFP. Instead,

insights into the chemical compositions of FeTFA and FePFP were obtained by the FAB-MS technique.

Low-resolution (LR) FAB-MS of FeTFA detected $(M + H)^+$ ions at $m/z = 1{,}416.5$ (31%) and m/z

$= 1{,}303.4$ $(M + H - TFA$, 36%). High-resolution (HR) FAB-MS (mass tolerance: $\pm$ 5 mmu) of FeTFA

detected $C_{18}F_{27}{}^{56}Fe_6O_{22}$. The m/z values of the calculated and experimental values were consistent

$(m/z_{calcd} = 1416.4546, m/z_{found} = 1416.4544)$. Fe has several stable isotopes, namely, ^{56}Fe: 91.75%,

^{54}Fe: 5.85%, ^{57}Fe: 2.12%, and ^{58}Fe: 0.28%. The HR FAB-MS measurements also yielded an isotopic

peak at $m/z = 1414.4549$, indicating the $C_{18}F_{27}{}^{54}Fe^{56}Fe_5O_{22}$ complex.

The LR and HR FAB-MS of FePFP detected $(M)^+$ ions at $m/z = 1{,}866.5$ (59%), $m/z = 1{,}703.5$ (M

$-$ PFP, 68%), m/z_{found} 1866.4264 $(m/z_{calcd}$ for $C_{27}F_{45}{}^{56}Fe_6O_{22} = 1866.4259)$, and 1703.4440 $(m/z_{calcd}$ for

M $-$ PFP). The soft ionization technique of FAB-MS generally yields a protonated cation, $[M + H]^+$.

Importantly, the corresponding intact cation M^+ is often observed [29]. In the HR FAB-MS

measurements, an isotope peak was also detected at m/z = 1864.4312 (indicating $C_{27}F_{45}{}^{54}Fe^{56}Fe_5O_{22}$).

Unfortunately, the strong paramagnetic properties of FeTFA and FePFP prevented insights into their chemical structures by nuclear magnetic resonance (NMR) (Fig. S3), so that the coordination number could not be determined from the Job plot [30]. However, from the results of Section 2, we concluded that both synthesized FeTFA and FePFP were hexanuclear complexes. Assuming that both complexes possess symmetrical structures and $CF_3CO_2{}^-$-counter ions, the chemical formulas of FeTFA and FePFP were estimated as $C_{16}F_{24}O_{20}Fe_6 \cdot CF_3CO_2$ and $C_{24}F_{40}O_{20}Fe_6 \cdot CF_3CF_2CO_2$, respectively.

To date, several mono- and polynuclear trifluoroacetate complexes have been reported in the literature. For instance, Adibi et al. [31] reported a mononuclear iron trifluoroacetate (Fe(TFA)$_3$). A tetranuclear zinc–TFA complex (known as ZnTAC24) is commercially available [32], and Guntlin et al. used a trinuclear trifluoroacetate complex as a precursor in the preparation of popcorn-shaped Wüstite [33]. Hence, the observation of polynuclear trifluoroacetate complexes in the present study is not surprising.

3.   Combustion inhibition efficiency of Fe-SCPFCs

The combustion inhibition efficiency was evaluated by measuring the downward flame spread

rates (DFSR) over a thermally thin filter paper adsorbed with a uniformly dispersed suppressant.

Cellulose is a well-known and typical solid combustible material, and the cellulose combustion

method is an established technique for measuring combustion inhibition efficiency. For instance, an

earlier work investigated the combustion inhibition ability of sodium bicarbonate by measuring the

flame spread rates of filter papers adsorbed with sodium bicarbonate and sodium carbonate [34].

McCater compared the downward spread rates of thermally thin cellulosic fuels containing 185

inorganic compounds [35]. Elsewhere, Koshiba et al. reported the downward spread rates of thermally

thin filter papers containing transition metal compounds [36]. The decomposition is limited at high-

temperature fuel surfaces. If the combustion inhibitors do not affect pyrolysis or the degradation

process of the solid fuel, the suppression efficiency does not significantly differ between combustion

inhibitors discharged onto a burning fuel and those adsorbed on the solid fuel [37]. The major

drawback of this method is the formation of suppressant crystals on the paper surfaces, which change

the dispersion of the adsorbed suppressants from uniform to heterogeneous. However, as will be noted

in Section 3.2, we were able to prepare homogeneously adsorbed samples.

Data from related studies suggest that the upward flame spread rate of a solid fuel (even a thermally

thin one) is generally unsteady [38], reflecting the co-occurrence of flame propagation, buoyant

convection, and diffusive gas transport. By contrast, the DFSR is generally reproducible [39]. In actual

solid fuel combustion, the upward flame propagation should be considered, but in the present study,

22

the experimentally measured DFSRs obtained reproducible results on suppression efficiency.

The downward flame spreading of thermally thin fuels is typically calculated by Eq. (1) [40]:

$$U = \frac{\sqrt{2}\lambda}{\rho_s c_p \delta}\left(\frac{T_f - T_v}{T_v - T_\infty}\right),\tag{1}$$

where U, λ, ρ_s, c_p, and δ represent the DFSR, gas phase thermal conductivity, solid fuel density, fuel

heat capacity, and solid fuel thickness, respectively. T_f, T_v, and T_∞ denote the flame, vaporization, and

ambient temperature, respectively. As explained below, all variables except T_f can be regarded as

constant, because the suppressants were adsorbed at low concentrations on the filter papers.

3.1 Materials and chemicals

FeTFA and FePFP were used as prepared. The reference chemicals $FeCl_3$ (>99.0%) and ADP

(>99.0%) were used as received. The suppressants were dissolved in dry alcohol (>99.5%). Hardened

filter papers (No. 4A, >99% cellulose, [41]) with a uniform thickness of 0.12 mm, a density of 96 g

m^{-2}, and an ash content of 0.025% were purchased from Tokyo Roshi Kaisha, Ltd. (Japan).

3.2 Sample preparation methods

Each suppressant was adsorbed on rectangular filter papers as described in a previous study [42].

First, the round hardened filter paper was cut into rectangular pieces of length 120.0 mm and width 5.0 mm. The cut paper was dried in a vacuum desiccator for >48 h and then weighed (W_0). The dry rectangular pieces were immersed in the ethanol solutions of the suppressants for the desired times. The rectangular piece was dried in a vacuum desiccator for >48 h and subsequently weighed (W_s). Scanning electron microscopy (SEM) observations verified no agglomeration of any suppressant on the filter papers, confirming that the suppressants were homogeneously adsorbed on the filter paper samples.

The concentration of the adsorbed suppressant (C_k) per unit weight of the rectangular sample was calculated as

$$C_k = \left(\frac{W_s - W_0}{M_k}\right)/W_0, \qquad (2)$$

where M_k denotes the molar mass of suppressant k.

3.3 Experimental details

The experimental apparatus of the suppression trials is shown in Fig. 6. The same apparatus was employed in a previous study [42]. The transparent acrylic tube was 300 mm high and 80 mm in diameter. The sample piece was vertically fixed with the sample holder in the tube. Air was then passed upward through a mass-flow controller (flow rate: 5.0 dm^3 min^{-1}, laminar, dry: H_2O < 15 ppm). The DFSR generally depends on various experimental parameters (e.g., gravity, experimental pressure, and oxygen concentration) [43]. However, as all current experiments were performed under the same conditions (an air atmosphere under atmospheric pressure), we could directly compare the DFSRs among the samples.
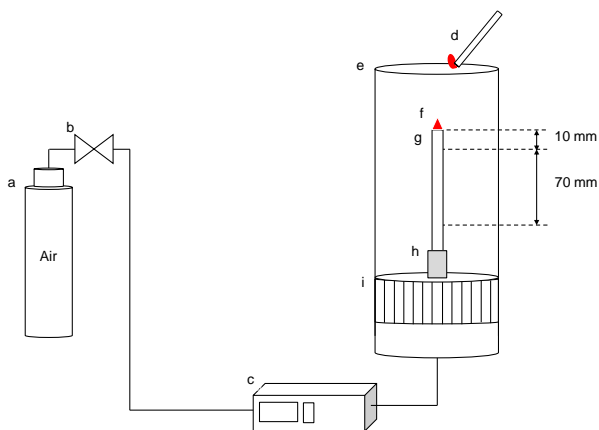
Figure 6

Schematic of the experimental apparatus for the suppression trials: (a) air cylinder, (b) valve, (c) mass-flow controller, (d) small pilot flame, (e) transparent acrylic tube, (f) flame, (g) filter paper sample, (h) sample holder, and (i) flow conditioner.

The upper edge of the sample piece was kindled with a small pilot flame. To avoid any effect of the small pilot flame, the DFSR was determined by measuring the time during which the flame edge propagated downward from a line 10 mm below the top of the sample piece to a line 80 mm below the top.

The normalized DFSR, V_k, is defined as

$$V_k = \frac{U_k}{U_0},\tag{3}$$

where U_k and U_0 represent the DFSRs of the sample adsorbed with suppressant k and a pure paper sample, respectively. Within the range $1 > V_k \geq 0$, smaller V_k indicates higher flame-suppressing efficiency. When $V_k = 0$, the fire is extinguished, and when $V_k > 1$, combustion is enhanced.

3.4 Experimental results

Figure 7a plots the normalized DFSRs as functions of FeTFA and FePFP concentration. In this figure, the error bars denote one standard deviation. As a reference, the normalized DFSRs versus the

ADP and FeCl$_3$ concentrations are plotted in Fig. 7b. Note that as mentioned above, the filter papers

with each suppressant were prepared and burned under dry conditions; thus, the influences of water

on the DFSRs were negligible in this study.
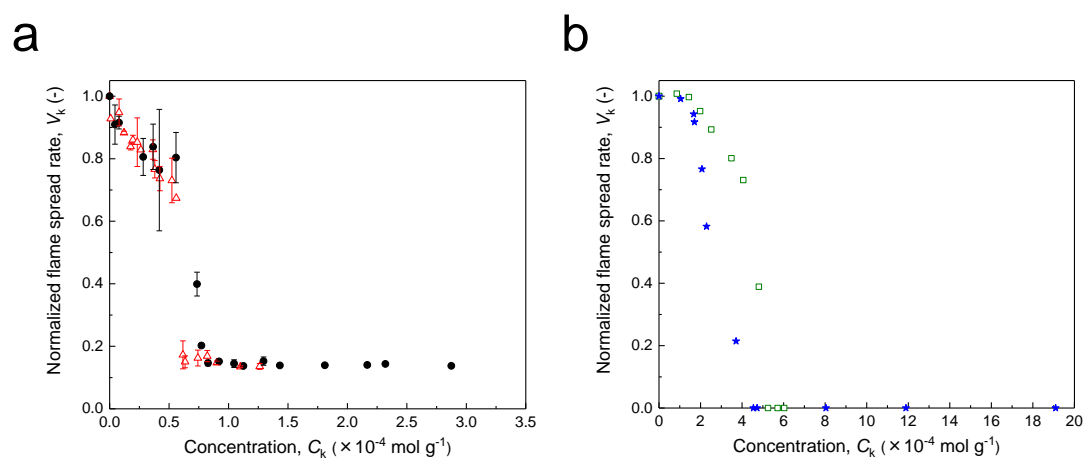
a

b

Figure 7

Normalized downward flame spreading rates, V_ks, as functions of suppressant concentration: (a)

FeTFA (closed circles) and FePFP (open triangles) and (b) ADP (open squares) and FeCl$_3$ (closed

stars). Error bars represent one standard deviation. Smaller V_k values indicate stronger combustion

inhibition efficiency. Note the different scales of the horizontal axes.

As shown in Fig. 7b, both V_{ADP} and V_{FeCl3} gradually decreased with increasing concentration,

eventually reaching 0 (i.e., fire extinction) at 5.3×10^{-4} mol g^{-1} and 4.5×10^{-4} mol g^{-1}, respectively

[7]. These concentrations are called the minimum extinction concentrations (MECs) of ADP and $FeCl_3$.

No glowing was observed in the tested concentration ranges of ADP and $FeCl_3$, and no re-ignition was noticed above their MECs.

The V_{FeTFA} and V_{FePFP} values decreased more steeply at low concentrations than V_{ADP} and V_{FeCl3} (Fig. 7a). V_{FeTFA} and V_{FePFP} were minimized at $V_{FeTFA} = 0.15$ and $V_{FePFP} = 0.14$ at $C_{FeTFA} = 0.83 \times 10^{-4}$ mol g^{-1} and $C_{FeTFA} = 0.61 \times 10^{-4}$ mol g^{-1}, respectively. Note that over the tested concentration range ([FeTFA] and [FePFP] $= 0–3.0 \times 10^{-4}$ mol g^{-1}), the V_{FeTFA} and V_{FePFP} values plateaued and did not reach zero, meaning that FeTFA and FePFP could not extinguish the flame. The sample pieces burned below at $C_{FeTFA} = 0.83 \times 10^{-4}$ mol g^{-1} and $C_{FePFP} = 0.61 \times 10^{-4}$ mol g^{-1}, whereas glowing (flameless) was observed at $C_{FeTFA} \geq 0.83 \times 10^{-4}$ mol g^{-1} and $C_{FePFP} \geq 0.61 \times 10^{-4}$ mol g^{-1}. The V_{FeTFA} and V_{FePFP} values might reach zero at higher concentrations of $C_{FeTFA} >$ ca. 2.9×10^{-4} mol g^{-1} and $C_{FePFP} >$ ca. 1.4×10^{-4} mol g^{-1}. Unfortunately, samples with such high concentrations were prevented by the adsorption limits of the FeTFA and FePFP complexes on the filter paper. The limit defines the concentration at which the weight of the filter paper with the complex no longer increases. FeTFA and FePFP might extinguish the flame if the adsorption concentration could be enhanced beyond the adsorption limit.

4. Combustion inhibition mechanisms of Fe-SCPFCs

When a flame propagates, volatile fuel vapors are pyrolytically produced in the preheated zone of the sample piece, resulting in a diffusion flame [44]. Heat transfer from the flame to the unburned cellulosic fuel yields flame inhibitors (i.e., inhibitor-derived vapors) and flammable fuel vapors.

In the condensed phase, if the Fe-SCPFCs hamper the pyrolysis of cellulosic fuel and/or oxidative degradation of the residual char (i.e., burnout), they will hinder the generation of volatile fuel vapors, eventually decreasing the flame spread rate. If Fe-SCPFCs decompose at low temperatures and behave as flame inhibitors in the gas phase, they will (along with fuel vapors) reduce the flame spread rate. Consequently, both condensed and gas phase inhibition effects were observed in the combustion test, which is one disadvantage of the method. Thus, the phase in which the Fe-SCPFCs exerted their inhibition effects was not determinable from the combustion test results alone.

A fundamental insight into the inhibition phase is crucial for elucidating the inhibition mechanism [36]. A TG analysis provides useful information on solid phase reactions. In earlier studies, the degradation mechanisms of solid cellulosic fuels were determined by monitoring the sample weight loss/gain as a function of temperature in TG analyses. For instance, Xian et al. researched the pyrolysis pathways of solid cellulosic fuels containing inorganic compounds (potassium chloride and copper (II) sulfate) in a TG analysis, and reported that the decomposition temperatures of solid fuels depend

on their salt concentration [45]. Koshiba et al., who investigated the degradation of cellulose, demonstrated that the decomposition temperatures shift toward higher temperatures in the presence of metallocenes [7].

4.1 Materials and chemicals

FeTFA and FePFP were used as prepared. Fine cellulose powder (<20 μm, >99.0%, Sigma–Aldrich) was dried in a vacuum desiccator for at least 48 h.

4.2 Sample preparation methods for TG

In a dry N_2-filled glovebox, the dry FeTFA and FePFP were well mixed with cellulose. As listed in Table 1, the concentrations of the complexes in the TG samples were relatively low (FeTFA/cellulose sample: C_{FeTFA} = 0.34 × 10^{-4} and 1.13 × 10^{-4} mol g^{-1}; FePFP/cellulose sample: C_{FePFP} = 0.36 × 10^{-4} and 1.09 × 10^{-4} mol g^{-1}). Each former concentration (entries 1 and 3 in Table 1) was lower than the concentration at which U plateaued, whereas each latter concentration (entries 2 and 4 in Table 1) was the complex concentration at which U plateaued (see Fig. 7). Each mixed sample was prepared at ca. 100 mg to avoid concentration bias of these complexes in the TG samples. From each 100-mg preparation, 2 mg was weighed into an alumina pan in a dry N_2-filled glovebox. The TG

measurements were collected three times for each sample, and no significant differences were observed. We further verified no significant differences in the TG curves of samples weighed in aluminum and alumina pans.

Table 1 FeTFA and FePFP concentrations in the TG analysis samples (see Figs. 9 and 10).

Entry	Sample	Suppressant concentration C_k (mol g^{-1})
1	FeTFA/cellulose	0.34×10^{-4}
2	FeTFA/cellulose	1.13×10^{-4}
3	FePFP/cellulose	0.36×10^{-4}
4	FePFP/cellulose	1.09×10^{-4}

Researchers have long debated the decomposition/combustion processes of cellulose at high temperatures. Nevertheless, the following main steps are non-contentious [46]: pyrolysis of cellulose at ca. 300 °C, which occurs under anaerobic atmospheres (Step 1), and residual char combustion at ca. >430 °C, which occurs under aerobic atmospheres (Step 2). In the present study, dry N_2 (>99.99%) and air were purged over the ranges of r.t.–400 °C and 400–600 °C, respectively, at a flow rate of 5.0 $\times 10^{-2}$ dm^3 min^{-1}.

The TG curves were obtained using a Shimadzu DTG-60 instrument (Japan) via a Shimadzu TA-60WS data processer (Japan) at a heating rate of 10 °C min^{-1}. Prior to measurements, the instrument

was calibrated using indium, tin, and zinc standards.

4.3 TG results

The TG and DTG curves of pure cellulose and FeTFA/cellulose are shown in Figs. 8 and 9, respectively. Pure cellulose exhibited a one-step weight loss. The onset temperature T_o was ca. 310 °C, which corresponds to the cellulose pyrolysis temperature [46]. In this study, the onset temperature was defined as the intersection point of the tangent to the DTG peak with the extrapolated baseline.
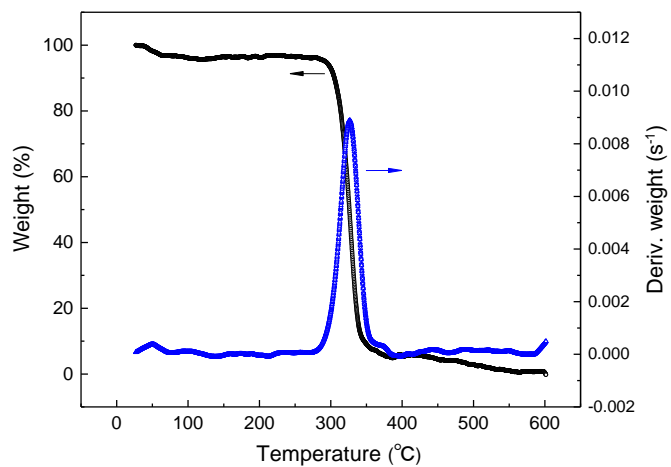

Figure 8

TG curves of pure cellulose (heating rate: 10 °C min^{-1}, purge gas: N_2 (r.t.–400 °C) and air (400–600 °C) (crucible: open alumina, initial sample weight: ca. 2 mg).

a

b
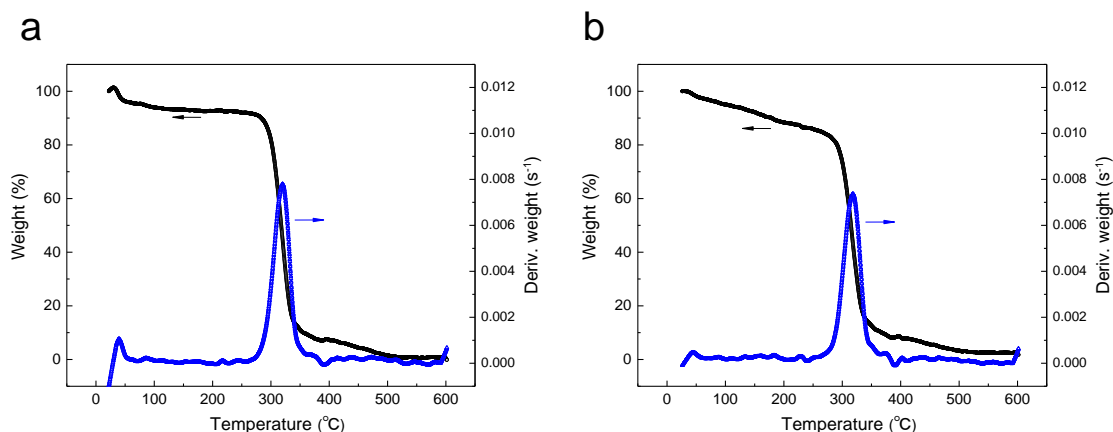
Figure 9

TG curves (heating rate: 10 °C min^{-1}, purge gas: N$_2$ (r.t.–400 °C) and air (400–600 °C), (crucible: open alumina, initial sample weight: ca. 2 mg). (a) Black circles: FeTFA/cellulose sample with C_{FeTFA} = 0.34 × 10^{-4} mol g^{-1} (Entry 1 of Table 1). (b) Blue triangles: FeTFA/cellulose sample with C_{FeTFA} = 1.13 × 10^{-4} mol g^{-1} (Entry 2 of Table 1).

The TG curves of the FeTFA/cellulose samples exhibited two weight losses. The first weight loss at ca. <300 °C was attributed to the decomposition of FeTFA (see Section 4.5). The weight loss differences in the curves of Entries 1 and 2 at < 300 °C are explained by differences in the FeTFA weights in each sample. The second weight loss was related to cellulose pyrolysis. The TG curves of FeTFA at both concentrations showed no significant differences in T_o. The residual weight (W_r) of pure cellulose was 0.4%, and those of the FeTFA/cellulose samples with C_{FeTFA} = 0.34 × 10^{-4} and

33

$C_{\text{FeTFA}} = 1.13 \times 10^{-4}$ mol g^{-1} were 0.4% and 2.3%, respectively.

Like the curves of FeTFA-containing cellulose, the TG and DTG curves of the FePFP/cellulose samples (Fig. 10) displayed no significant differences in T_o among the pure cellulose and both FePFP/cellulose samples. The W_r values of the FePFP/cellulose samples with $C_{\text{FePFP}} = 0.36 \times 10^{-4}$ and 1.09×10^{-4} mol g^{-1} were 0.0%.
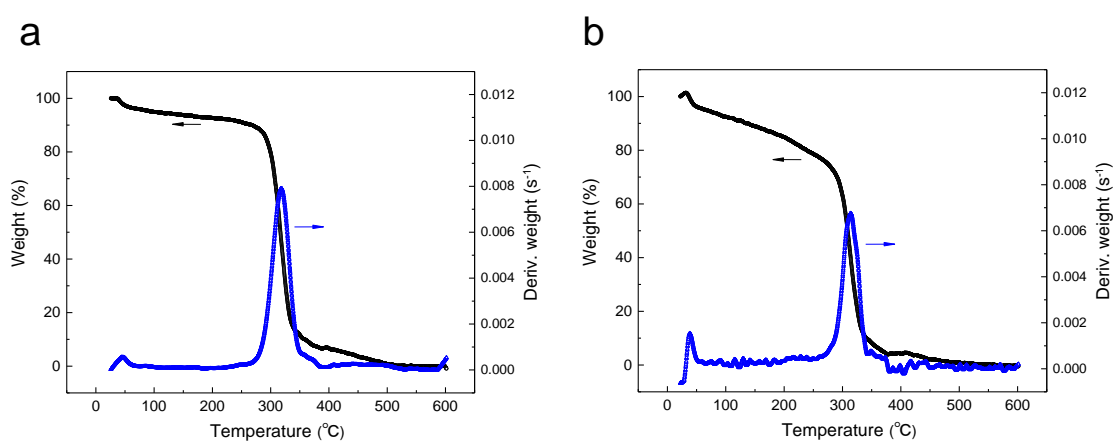

Figure 10

TG curves (heating rate: 10 °C min^{-1}, purge gas: N$_2$ (r.t.–400 °C) and air (400–600 °C) (crucible: open alumina, initial sample weight: ca. 2 mg). (a) FePFP/cellulose sample with $C_{\text{FePFP}} = 0.36 \times 10^{-4}$ mol g^{-1} (Entry 3 of Table 1). (b) FePFP/cellulose sample with $C_{\text{FePFP}} = 1.09 \times 10^{-4}$ mol g^{-1} (Entry 4 of Table 1).

The similar T_o and W_r values in the TG results indicate that FeTFA and FePFP (and their pyrolysis products) did not impair the cellulose pyrolysis, nor hamper the char combustion. From the results of this section, which are linked to the solid phase reactions of the perfluorocarboxylato complexes with cellulose, together with the findings of the suppression trials in Section 3, we conclude that both FeTFA and FePFP exert their combustion inhibition effects not in the solid phase, but rather in the gas phase through a process of elimination.

4.4 TG-MS measurement methods

Judging from the results of Section 4.3, a clear insight into the gas phase pyrolysis products of FeTFA and FePFP is essential for elucidating their combustion inhibition mechanisms. In this study, the decomposition mechanisms of pure FeTFA and FePFP were elucidated by the simultaneous TG-MS technique.

Measurements were performed by a quadruple mass spectrometer (GCMS-QP2010 SE, Shimadzu, Japan) connected to a thermogravimetric analyzer (STA2500 Regulus, Netzsch, Germany). Pure complexes (ca. 1 mg) were loaded into alumina pans and heated from r.t. to 600 °C at 10 °C min^{-1} under a helium flow rate of 7.0×10^{-2} dm^3 min^{-1}. The ionization method was electron ionization.

4.5 TG-MS results and combustion inhibition mechanisms

As expected, the perfluorocarboxylato complexes (as-is) and their derivatives (i.e., iron species) were not detected by the mass spectrometer, because they agglomerated before reaching the detector. The major pyrolysis products in the gas phase were H_2O ($m/z = 18$), HF ($m/z = 20$), CO ($m/z = 28$), CO_2 etc. ($m/z = 44$), and CF_3 ($m/z = 69$). As such, only F-derivatives are addressed in this section.

Fig. 11 plots the generation rates R_k of HF and CF_3 as functions of temperature, together with the TG curves of FeTFA and FePFP. The generation rate is calculated as

$$R_k = \frac{W_k}{W_c} \times 100, \tag{4}$$

where W_k and W_c denote the weights of generated gas k and the complex loaded in the alumina pan, respectively. At least five decomposition steps were observed in the curve of FeTFA. No significant weight loss appeared at 73 °C (the boiling point of TFA), strongly suggesting that no free TFA resided on the FeTFA sample.
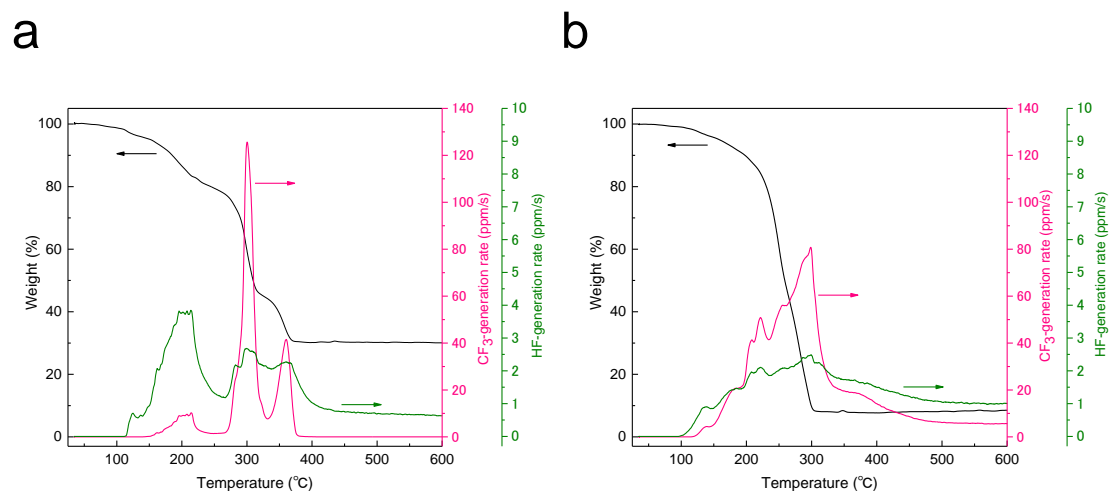
Figure 11

HF- and CF$_3$-generation rates (green and pink, respectively) and weight loss curves (black) as

functions of temperature: (a) FeTFA and (b) FePFP. The ppm concentrations are based on weight.
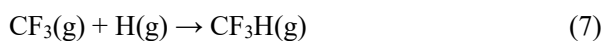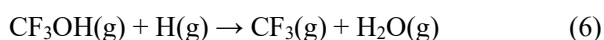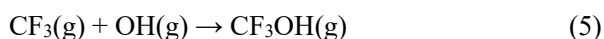
Heating rate: 10 °C min^{-1}, purge gas: He (r.t.–600 °C), crucible: open alumina.

Wörle et al. [47] synthesized iron (III) trifluoroacetate, Fe(TFA)$_3$, by a different synthesis approach
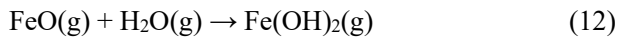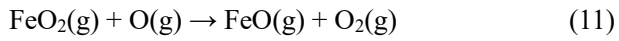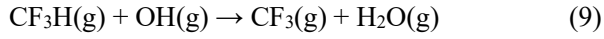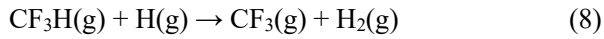
to ours. They reported an infinite chain structure of Fe(TFA)$_3$. Their TG-MS (purge gas: Ar) and XRD

analyses revealed that (i) Fe(TFA)$_3$ decomposed at 300 °C with a 52% weight loss attributable to the

formation of FeF$_2$(TFA), (ii) FeF$_3$ was generated at ca. 360 °C, causing a 19% weight loss (at that

temperature, the total weight loss from Fe(TFA)$_3$ to FeF$_3$ was 71%), and (iii) F-compounds (i.e., CF$_3$

ad F), CO$_2$, and CO were the decomposition products in the gas phase (detected by a mass

spectrometer). Guntlin et al. synthesized a trinuclear iron trifluoroacetate complex, Fe$_3$OTFA [33], and

37

found four decomposition stages in the TG-MS curves, with weight losses of 26% and 14% at 300 and

340 °C, respectively. The key decomposition products were CF_3 and COF_2. The findings of the earlier

and present studies suggest that the TG behavior and decomposition products largely depend on the

synthesis scheme and structure of the iron perfluorocarboxylato complexes.

In the present study, the total concentrations of generated HF for FeTFA and FePFP at r.t. –600 °C

were determined to be 4.2×10^3 and 4.2×10^3 ppm, respectively. Clearly, the generated HF

concentrations for FeTFA and FePFP were identical and low. In contrast, the total concentrations of

generated CF_3 for FeTFA and FePFP at r.t. –600 °C were 2.4×10^4 and 6.2×10^4 ppm, respectively,

one order of magnitude higher than the HF concentration, and 2.5-fold higher for FePFP than for

FeTFA.

The combustion inhibition process is illustrated in Fig.12. Fukaya et al.'s ab initio study

demonstrated that in radical recombination mechanisms, CF_3 is a more important radical than F (or

HF) [48]. Fukaya et al. [12] and Linteris et al. [49], who proposed fire suppression processes of

trifluoromethyl radical and iron species, suggested the following chemical suppression mechanisms:

$$CF_3(g) + OH(g) \rightarrow CF_3OH(g) \qquad (5)$$

$$CF_3OH(g) + H(g) \rightarrow CF_3(g) + H_2O(g) \qquad (6)$$

$$CF_3(g) + H(g) \rightarrow CF_3H(g) \qquad (7)$$

$$CF_3H(g) + H(g) \rightarrow CF_3(g) + H_2(g) \qquad (8)$$

$$CF_3H(g) + OH(g) \rightarrow CF_3(g) + H_2O(g) \qquad (9)$$

$$Fe(g) + O_2(g) + M(g) \rightarrow FeO_2(g) + M(g) \qquad (10)$$

$$FeO_2(g) + O(g) \rightarrow FeO(g) + O_2(g) \qquad (11)$$

$$FeO(g) + H_2O(g) \rightarrow Fe(OH)_2(g) \qquad (12)$$

$$Fe(OH)_2(g) + H(g) \rightarrow FeOH(g) + H_2O(g) \qquad (13)$$

$$FeOH(g) + H(g) \rightarrow FeO(g) + H_2(g) \qquad (14)$$

$$FeOH(g) + H(g) \rightarrow Fe(g) + H_2O(g) \qquad (15)$$

$$FeO(g) + O(g) \rightarrow Fe(g) + O_2(g) \qquad (16)$$
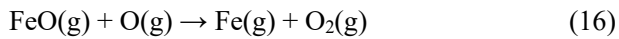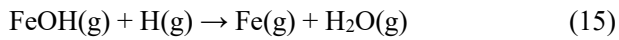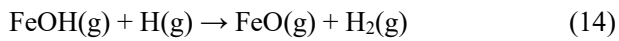
where M denotes the third body. As shown here, the trifluoromethyl radical and active iron species inhibit the catalytical recombination of hydroxyl, hydrogen, and oxygen radicals. The different combustion inhibition abilities described in Section 3 are probably explained by different CF_3 generation capabilities and eases of complex decomposition. Unfortunately, although FeTFA and FePFP showed high combustion inhibition ability at low concentrations, they could not extinguish the flame at high concentrations (see Fig. 7). This failure is probably due to the agglomeration/condensation of active metal species produced from the polynuclear complexes in the
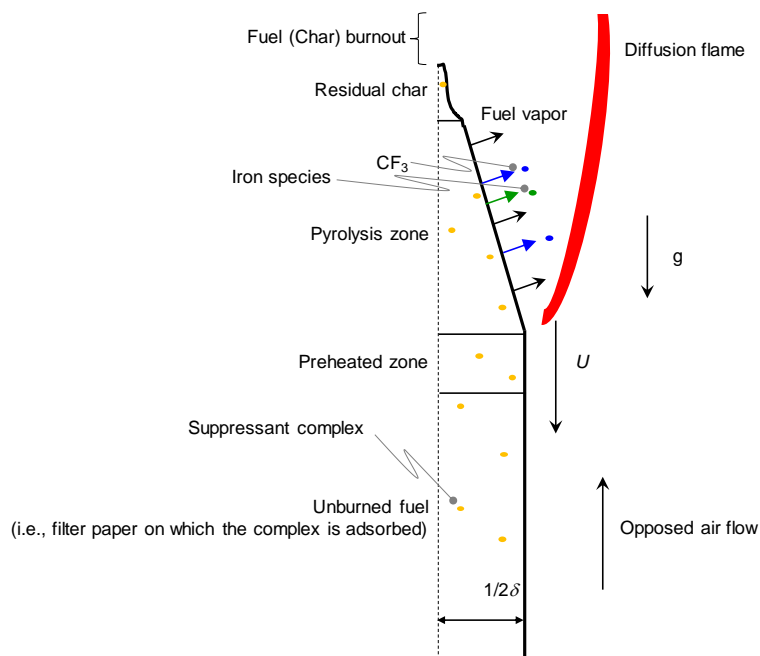
gas phase.

Figure 12

Schematic of downward flame spread over the thin filter paper adsorbed with the suppressant complex; δ, U, and g denote the thickness of the filter paper sample, downward flame spread rate, and acceleration due to gravity, respectively. The orange, green, and blue circles represent the adsorbed suppressant complex, CF_3 radicals, and iron species, respectively.

4.6 Remarks

As noted in Section 2.4, the chemical structures of FeTFA and FePFP were not determinable by

single-crystal XRD, owing to the high hygroscopicity of the complexes. Furthermore, the starting reactants of FeTFA and FePFP (the as-is TFA and PFP, respectively) are somewhat toxic to aquatic animals such as fishes and aquatic invertebrates. Further research on the toxicity of Fe-SCPFCs is necessary for their practical application as fire-extinguishing agents.

Prior to our study, the combustion inhibition ability of Fe-SCPFCs had not been reported. In addition, the high water solubility of the synthesized FeTFA and FePFP is a distinct advantage, meaning that Fe-SCPFCs can be applied as effective additives (or co-additives) of water-based fire-extinguishing agents. Notwithstanding the above-mentioned limitations, this study lays the groundwork for future preparations of new perfluorocarboxylate-based flame inhibitors.

5. Conclusions

In this work, we prepared iron trifluoroacetate and iron pentafluoropropionate and investigated their combustion inhibition efficiencies. The key findings are summarized below.

1. UV−Vis and FT-IR measurements confirmed that the TFA and PFP ligands are coordinated with iron ions in bridging form. XRF measurements and Cl⁻ elution tests revealed the absence of Cl⁻ ions in the synthesized FeTFA and FePFP complexes. The LR and HR FAB-MS measurements

41

demonstrated that FeTFA and FePFP are hexanuclear complexes with chemical formulas $C_{18}F_{27}O_{22}Fe_6$ and $C_{27}F_{45}O_{22}Fe_6$, respectively.

2. The fire suppression trials experimentally demonstrated that although FeTFA and FePFP could not extinguish the flames over the tested concentration range, their combustion inhibition efficiency exceeded that of ADP, an active substance of a powder fire-extinguishing agent, at low suppressant concentrations. In addition, FePFP exerted a dramatically higher inhibition effect than FeTFA.

3. TG measurements confirmed that both FeTFA and FePFP generated their combustion inhibition effects not in the solid phase, but in the gas phase. As revealed in the TG-MS measurements, the major gas-phase decomposition product of FeTFA and FePFP was CF_3. The major difference between FeTFA and FePFP was the generated CF_3 concentration. This difference probably accounts for the different inhibition abilities of FeTFA and FePFP.

This study provided the first demonstration of the combustion inhibition efficiency of Fe-SCPFC ($n = 1$ and $n = 2$). The findings will assist the development of a novel phosphorus-free, iron- and short-chain perfluorocarboxylate-based fire-extinguishing agent, which can potentially reduce fire-related fatalities and economic losses.

CRediT author statement

Yusuke Koshiba: Conceptualization, Methodology, Data curation, Writing–Original draft, Writing–Review & Editing, Supervision, Project administration, Funding acquisition. **Yuji Tsunokuma**: Methodology, Investigation, Data curation. **Hideo Ohtani**: Data curation. All the authors were responsible for data collection and have approved the final version of the manuscript.

Conflict of interest

None of the authors have any conflicts of interest to declare.

Acknowledgments

References

1. M.J. Gollner, Detection and suppression of fires: a cornerstone of fire protection engineering, Fire Technol. 52 (2016) 1193–1196. https:// doi:10.1007/s10694-010-0185-6

2. European Commission, Critical raw materials, 2017. https://ec.europa.eu/growth/sectors/raw-materials/specific-interest/critical_en (accessed May 2020).

3. D.P., Van Vuuren, A.F. Bouwman, A.H.W. Beusen, Phosphorus demand for the 1970–2100 period: A scenario analysis of resource depletion, Glob. Env. Change 20 (2010) 428–439. https://doi:10.1016/j.gloenvcha.2010.04.004

4. L. Cisse, T. Mrabet, World phosphate production: Overview and prospects, Phosphorus Res. Bull. 15 (2004) 21–25. https://doi.org/10.3363/prb1992.15.0_21

5. U.S. Geological Survey, U.S. Department of the Interior, Mineral Commodity Summaries, 2020, https://www.usgs.gov/ (accessed May 2020).

6. X. Ni, X. Wang, S. Zhang, M. Zhao, Experimental study on the performance of transition metal ions modified zeolite particles in suppressing methane/air coflowing flame on cup burner, J. Fire Sci. 32 (2014) 417–430. https://doi.org/10.1177/0734904114529402

7. Y. Koshiba, Y. Takahashi, H. Ohtani, Flame suppression ability of metallocenes (nickelocene, cobaltocene, ferrocene, manganocene, and chromocene), Fire Saf. J. 51 (2012) 10–17. https://doi.org/10.1016/j.firesaf.2012.02.008

8. G.T. Linteris, M.D. Rumminger, V. Babushok, W. Tsang, Flame inhibition by ferrocene and blends of inert and catalytic agents, Proc. Combust. Inst. 28 (2000) 2965–2972. https://doi.org/10.1016/S0082-0784(00)80722-5

9. Y. Koshiba, T. Tomita, H. Ohtani, Oil-in-water microemulsion containing ferrocene: A new fire suppressant, Fire Saf. J. 98 (2018) 82–89. https://doi.org/10.1016/j.firesaf.2018.04.005

10. Y. Koshiba, S. Okazaki, H. Ohtani, Experimental investigation of the fire extinguishing capability of ferrocene-containing water mist, Fire Saf. J. 83 (2016) 90–98. https://doi.org/10.1016/j.firesaf.2016.05.006

11. Y. Koshiba, H. Ohtani, Extinguishing pool fires with aqueous ferrocene dispersions containing gemini surfactants, J. Loss Prev. Process Ind. 40 (2016) 10–16. https://doi.org/10.1016/j.jlp.2015.11.029

12. H. Fukaya, T. Ono, T. Abe, Theoretical study of reaction of trifluoromethyl radical with hydroxyl and hydrogen radicals, J. Comput. Chem. 19 (1998) 277–289. https://doi.org/10.1002/(SICI)1096-987X(199802)19:3<277::AID-JCC2>3.0.CO;2-Q

13. G. LeFort, A.W. Marshall, M. Pabon, Evaluation of surfactant enhanced water mist performance, Fire Technol. 45 (2009) 341–354. https://doi.org/10.1007/s10694-008-0068-2

14. S.A. Magrabi, B.Z. Dlugogorski, G.J. Jameson, A comparative study of drainage characteristics in AFFF and FFFP compressed-air fire-fighting foams, Fire Saf. J. 37 (2002) 21–52. https://doi.org/10.1016/S0379-7112(01)00024-8

15. United Nations, Stockholm Convention, Protecting human health and the environment from persistent organic pollutants, 2019. http://chm.pops.int/Home/tabid/2121/Default.aspx (accessed May 2020).

16. K. Prevedouros, I.T. Cousins, R.C. Buck, S.H. Korzeniowski, Sources, fate and transport of perfluorocarboxylates, Environ. Sci. Technol. 40 (2006) 32–44. https://doi.org/10.1021/es0512475

17. J.W. Martin, S.A. Mabury, K.R. Solomon, D.C.G. Muir, Bioconcentration and tissue distribution of perfluorinated acids in rainbow trout (Oncorhynchus mykiss), Environ. Toxicol. Chem., 22 (2003) 196–204. https://doi.org/10.1002/etc.5620220126

18. R.G. Pearson, Hard and soft acids and bases, J. Am. Chem. Soc. 85 (1963) 3533–3539. https://doi.org/10.1021/ja00905a001

19. Y. Koshiba, Y. Nakamura, D. Ito, T. Yokoyama, S. Okazaki, H. Nakagawa, T. Arai, Development of a durable fiber-optic oxygen sensor for harsh underground environments, Talanta 82 (2010) 1495–1499. https://doi.org/10.1016/j.talanta.2010.07.027

20. R. Yagi, K. Tsuji, Confocal micro-XRF analysis of light elements with Rh X-ray tube and its application for painted steel sheet, X-Ray Spectrom. 44 (2015) 186–189. https://doi.org/10.1002/xrs.2599

21. JIS K101, Testing methods for industrial water (2017) Tokyo.

22. L. Mayrand-Provencher, D. Rochefort, Origin and effect of impurities in protic ionic liquids based on 2-methylpyridine and trifluoroacetic acid for applications in electrochemistry, Electrochim. Acta 54 (2009) 7422–7428. https://doi.org/10.1016/j.electacta.2009.07.075

23. National Institute of Advanced Industrial Science and Technology (AIST), Spectral Database for Organic Compounds (SDBS), https://sdbs.db.aist.go.jp/sdbs/cgi-bin/cre_index.cgi (accessed May 2020).

24. R.L. Redington, Matrix-isolation spectra of ^{18}O-substituted trifluoroacetic acid monomers and vibrational assignments for related CF_3-containing molecules, Spectrochim. Acta Pt. A-Molec.

Spectr. 31 (1975) 1699–1705. https://doi.org/10.1016/0584-8539(75)80112-7

25. M. Nara, H. Torii, M. Tasumi, Correlation between the vibrational frequencies of the carboxylate group and the types of Its coordination to a metal Ion: An *ab Initio* molecular orbital study, J. Phys. Chem. 100 (1996) 19812–19817. https://doi.org/10.1021/jp9615924

26. G.B. Deacon, R.J. Phillips, Relationships between the carbon-oxygen stretching frequencies of carboxylato complexes and the type of carboxylate coordination, Coord. Chem. Rev. 33 (1980) 227–250. https://doi.org/10.1016/S0010-8545(00)80455-5

27. H. Wang, T.O. Hahn, C.J. Sung, C.K. Law, Detailed oxidation kinetics and flame inhibition effects of chloromethane, Combust. Flame 105 (1996) 291–307. https://doi.org/10.1016/0010-2180(95)00206-5

28. X. Cao, J. Ren, Y. Zhou, Q. Wang, X. Gao, M. Bi, Suppression of methane/air explosion by ultrafine water mist containing sodium chloride additive, J. Hazard. Mater. 285 (2015) 311–318. http://dx.doi.org/10.1016/j.jhazmat.2014.11.016

29. J.M. Miller, K. Balasanmugam, Characterization of metal complexes of 1,10-phenanthroline, 2,2'-bipyridine, and their derivatives by fast atom bombardment mass spectrometry, Can. J. Chem. 67 (1989) 1496–1500. https://doi.org/10.1139/v89-228

30. J.S. Renny, L.L. Tomasevic, E.H. Tallmadge, D.B. Collum, Method of continuous variations:

Applications of Job plots to the study of molecular associations in organometallic chemistry, Angew. Chem., Int. Ed. 52 (2013) 11998−12013. https://doi.org/10.1002/anie.201304157

31. H. Adibi, H.A. Samimi, M. Beugzadeh, Iron(III) trifluoroacetate and trifluoromethanesulfonate: Recyclable Lewis acid catalysts for one-pot synthesis of 3,4-dihydropyrimidinones or their sulfur analogues and 1,4-dihydropyridines via solvent-free Biginelli and Hantzsch condensation protocols, Catal. Commun. 8 (2007) 2119–2124. https://doi.org/10.1016/j.catcom.2007.04.022

32. Y. Hayashi, T. Ohshima, Y. Fujii, Y. Matsushima, K Mashima, A trifluoroacetic acid adduct of a trifluoroacetate-bridged μ_4-oxo-tetranuclear zinc cluster, $Zn_4(OCOCF_3)_6O \cdot CF_3CO_2H$: Synthesis under mild conditions and catalytic transesterification and oxazoline formation, Catal. Sci. Technol. 1 (2011) 230–233. https://doi.org/10.1039/C0CY00048E

33. C.P. Guntlin, S.T. Oshsenbein, M. Wörle, R. Erni, K.V. Kravchyk, M.V. Kovalenko, Popcorn-shaped Fe_xO (wüstite) nanoparticles from a single-source precursor: Colloidal synthesis and magnetic properties, Chem. Mater. 30 (2018) 1249−1256. https://doi.org/10.1021/acs.chemmater.7b04382

34. M. Izumikawa, T. Mitani, T. Noka, Burning Behavior of Paper Inhibited by $NaHCO_3$, J. Fire Sci. 4 (1986) 332−345. https://doi.org/10.1177/073490418600400503

35. R.J. McCater, Combustion inhibition of cellulose by powders: Preliminary data and hypotheses,

Fire Mater. 5 (1981) 66−72. https://doi.org/10.1002/fam.810050206

36. Y. Koshiba, S. Agata, T. Takahashi, H. Ohtani, Direct comparison of the flame inhibition efficiency of transition metals using metallocenes, Fire Saf. J. 73 (2015) 48–54. https://doi.org/10.1016/j.firesaf.2015.03.003

37. M. Izumikawa, T. Mitani, T. Niioka, Flame spread of paper sheets containing suppressants, Trans. Jpn. Soc. Mech. Eng. B 52 (1986) 1413–1419. https://doi.org/10.1299/kikaib.52.1413

38. P.D. Ronney, J.B. Greenberg, Y. Zhang, V. Roegner, Flame spread over thin solid fuels in partially premixed atmospheres, Combust. Flame 100 (1995) 474–484. https://doi.org/10.1016/0010-2180(94)00132-C

39. S. Bhattacharjee, C. Paolini, W. Tran, J.R. Villaraza, S. Takahashi, Temperature and CO_2 fields of a downward spreading flame over thin cellulose: A comparison of experimental and computational results, Proc. Combust. Inst. 35 (2015) 2665–2672. https://doi.org/10.1016/j.proci.2014.05.093

40. Society of Fire Protection Engineers, SFPE handbook of fire protection engineering, in: J.G. Quintiere (Ed.), Surface Flame Spread, third ed., 2002, pp. 2-246–2-257, Massachusetts.

41. JIS P3801, Filter paper (for chemical analysis) (1995), Tokyo.

42. Y. Koshiba, T. Haga, H. Ohtani, Flame inhibition by calcium compounds: Effects of calcium

compounds on downward flame spread over solid cellulosic fuel, Fire Saf. J. 109 (2019) 102865.

https://doi.org/10.1016/j.firesaf.2019.102865

43. S. Bhattacharjee, M. Bundy, C. Paolini, G. Patel, W. Tran, A novel apparatus for flame spread

study, Proc. Combust. Inst. 34 (2013) 2513–2521. https://doi.org/10.1016/j.proci.2012.05.076

44. T. Hirano, K. Saito, Fire spread phenomena: the role of observation in experiment, Prog. Energy

Combust. Sci. 20 (1994) 461–485. https://doi.org/10.1016/0360-1285(94)90001-9

45. S. Xian, H. Yuan, Huhetaoli, Y. Qi, P. Lv, Z. Yuan, Y. Chen, Characterization of the decomposition

behaviors of catalytic pyrolysis of wood using copper and potassium over thermogravimetric and

Py-GC/MS analysis, Energy 114 (2016) 636646. https://doi.org/10.1016/j.energy.2016.07.154

46. D. Shen, J. Ye, R. Xiao, H. Zhang, TG-MS analysis for thermal decomposition of cellulose under

different atmospheres, Carbohydr. Polym. 98 (2013) 514–521.

https://doi.org/10.1016/j.carbpol.2013.06.031

47. M. Wörle, C.P. Guntlin, L. Gyr, M.T. Sougrati, C.-H. Lambert, K.V. Kravchyk, R. Zenobi, M.V.

Kovalenko, Structural evolution of iron(III) trifluoroacetate upon thermal decomposition: Chains,

layers and rings, Chem. Mater. 32 (2020) 2482–2488.

https://doi.org/10.1021/acs.chemmater.9b05004

48. H. Fukaya, T. Ono, T. Abe, Ab initio molecular orbital study of reaction of pentafluoroethyl radical

with hydroxyl and hydrogen radicals, Bull. Chem. Soc. Jpn. 72 (1999) 207–211. https://doi.org/10.1246/bcsj.72.207

49. G.T. Linteris, M.D. Rumminger, V.I. Babushok, Catalytic inhibition of laminar flames by transition metal compounds, Prog. Energy Combust. Sci. 34 (2008) 288–329. https://doi.org/10.1016/j.pecs.2007.08.002

Figure captions

Figure 1

Estimated trends in average market prices of phosphate rocks from 2000 to 2020 (adapted from [5])

Figure 2

Chemical structures of (a) trifluoroacetic acid (TFA) and (b) pentafluoropropionic acid (PFP).

Figure 3

Appearance of synthesized (a) FeTFA (dark red hexahedron crystals in a dry N_2 purged vial) and (b)

FePFP (dark orange needle-like crystals in a dry N_2 purged vial).

Figure 4

FT-IR spectra (KBr, r.t.) of (a) FeTFA and (b) FePFP.

Figure 5

XRF spectra of (a) FeTFA and (b) FePFP (30.0 kV). The rhodium peaks are contributed by the Rh

tube.

Figure 6

Schematic of the experimental apparatus for the suppression trials: (a) air cylinder, (b) valve, (c) mass-

flow controller, (d) small pilot flame, (e) transparent acrylic tube, (f) flame, (g) filter paper sample, (h)

sample holder, and (i) flow conditioner.

Figure 7

Normalized downward flame spreading rates, V_ks, as functions of suppressant concentration: (a) FeTFA (closed circles) and FePFP (open triangles) and (b) ADP (open squares) and $FeCl_3$ (closed stars). Error bars represent one standard deviation. Smaller V_k values indicate stronger combustion inhibition efficiency. Note the different scales of the horizontal axes.

Figure 8

TG curves of pure cellulose (heating rate: 10 °C min^{-1}, purge gas: N_2 (r.t.–400 °C) and air (400–600 °C) (crucible: open alumina, initial sample weight: ca. 2 mg).

Figure 9

TG curves (heating rate: 10 °C min^{-1}, purge gas: N_2 (r.t.–400 °C) and air (400–600 °C), (crucible: open alumina, initial sample weight: ca. 2 mg). (a) Black circles: FeTFA/cellulose sample with C_{FeTFA} = 0.34×10^{-4} mol g^{-1} (Entry 1 of Table 1). (b) Blue triangles: FeTFA/cellulose sample with C_{FeTFA} = 1.13×10^{-4} mol g^{-1} (Entry 2 of Table 1).

Figure 10

TG curves (heating rate: 10 °C min^{-1}, purge gas: N$_2$ (r.t.–400 °C) and air (400–600 °C) (crucible: open alumina, initial sample weight: ca. 2 mg). (a) FePFP/cellulose sample with $C_{\text{FePFP}} = 0.36 \times 10^{-4}$ mol g^{-1} (Entry 3 of Table 1). (b) FePFP/cellulose sample with $C_{\text{FePFP}} = 1.09 \times 10^{-4}$ mol g^{-1} (Entry 4 of Table 1).

Figure 11

HF- and CF$_3$-generation rates (green and pink, respectively) and weight loss curves (black) as functions of temperature: (a) FeTFA and (b) FePFP. The ppm concentrations are based on weight. Heating rate: 10 °C min^{-1}, purge gas: He (r.t.–600 °C), crucible: open alumina.

Figure 12

Schematic of downward flame spread over the thin filter paper adsorbed with the suppressant complex; δ, U, and g denote the thickness of the filter paper sample, downward flame spread rate, and acceleration due to gravity, respectively. The orange, green, and blue circles represent the adsorbed suppressant complex, CF$_3$ radicals, and iron species, respectively.

Table caption

Table 1

FeTFA and FePFP concentrations in the TG analysis samples (see Figs. 9 and 10).

Scheme caption

Scheme 1

Synthesis methods of (a) FeTFA (water/TFA, reflux, 26 h) and (b) FePFP (water/PFP, reflux, 26 h).